

Cation vacancies creation propel pre-oxidation enhancing nickel hydroxide activity for highly efficient 5-hydroxymethylfurfural upgrading

Xiaoli Jiang^a, Xianhui Ma^b, Yanxia Liu^a, Lin Zhao^a, Yagang Zhang^{a,*}, Bo-Quan Li^{c,*}, Qiang Zhang^{d,*}

^a University of Electronic Science and Technology of China, School of Materials and Energy, Chengdu 611731, China

^b University of Science and Technology of China, School of Chemistry and Materials Science, Collaborative Innovation Center of Chemistry for Energy Materials(iChEM), Hefei 230026, China

^c Beijing Institute of Technology, Advanced Research Institute of Multidisciplinary Science, Beijing 100081, China

^d Tsinghua University, Department of Chemical Engineering, Beijing Key Laboratory of Green Chemical Reaction Engineering and Technology, Beijing 100084, China



ARTICLE INFO

Keywords:

5-hydroxymethylfurfural oxidation reaction
Cation vacancy
 $\text{Ni}^{3+}\text{-O}$ active species
Electro-catalyst

ABSTRACT

The 5-hydroxymethylfurfural oxidation reaction (HMFOR) is an energy-saving alternative for H_2 production due to the low thermodynamic potential. However, the comprehensive investigation into the dehydrogenation pre-oxidation and substrates adsorption on catalyst with vacancy has not been carried out. Herein, we report a unique strategy to create cation vacancies by *in situ* molybdenum removal in pre-catalyst. The resulting vacancy-enriched $\text{V}_{\text{Mo}}\text{-NiO}_x\text{H}_y$ catalyst enables a tripling promotion on current density than the pristine NiO_xH_y and delivers a much lower onset couple voltage than water splitting. The enhanced performance is attributed to the formation of $\text{Ni}^{3+}\text{-O}$ active substances induced by the vacancy manipulation pre-oxidation process, the optimized substrate adsorption, and the decorated Nickel electron coordination structure owing to the vacancy creation, which are evidenced by the operando spectroscopy measurements, density functional theory calculations, and X-ray absorption spectroscopy, respectively. This work shines new light on electro-catalysts design for value-added chemicals production via biomass upgrading.

1. Introduction

The increasing global energy demand and environmental pollution have motivated the rapid development of renewable and green energy storage and conversion technologies [1–3]. Electrochemical water splitting emerges as an attractive strategy to produce green hydrogen [4, 5]. Whereas the anodic oxygen evolution reaction (OER) is heavily sluggish in kinetics and seriously reduces the energy utilization efficiency of water splitting devices [5–7]. Owing to favorable thermodynamics, electrocatalytic conversion of biomass derivatives, such as furfural [8], furfuryl alcohol [9], 5-hydroxymethylfurfural (HMF) [10], and glucose [11] to replace OER provides a promising and accessible strategy for the acquisition of maximum current efficiency and generation of high value-added products simultaneously [12,13]. Among the numerous biomass derivatives, HMF can be served as the bridge between fossil-based chemicals and biomass. Because of the catalyzed production of multitudinous industrial value-added compounds, HMF has caught great industrial and scientific attention [14,15]. Of particular

importance is the oxidation product 2,5-furandicarboxylic acid (FDCA), which has a similar chemical structure to petroleum-based monomer terephthalic acid (TPA), presenting considerable potential as a substitute for the synthesis of degradable plastics [16]. Among the various routes, electrocatalytic HMF oxidation reaction (HMFOR) to produce FDCA has triggered a research boom due to the advantages of mild reaction conditions and avoiding strong oxidants using. By coupling HMFOR and hydrogen evolution reaction (HER), it is conducive to rationally lowering the energy consumption of hydrogen generation and leading to significant advances in both industrial production and scientific research [17,18]. Hence, a thorough understanding of the catalytic mechanism of HMFOR is crucial for the exploration of electrocatalysts with high catalytic performance.

The HMFOR process occurs on the sur-/interface of catalyst where facilitates the transportation and formation of reactants, intermediates, and products. Defects, widely existed in heterogeneous/amorphous nanomaterials, able to tune electronic structure and coordination environment of the electrocatalysts to alter the adsorption energy of the

* Corresponding authors.

E-mail addresses: ygzhang@uestc.edu.cn (Y. Zhang), libq@bit.edu.cn (B.-Q. Li), zhang-qiang@mails.tsinghua.edu.cn (Q. Zhang).

reactive species, consequently improving the electrocatalytic performance. For example, oxygen vacancies can act as reaction sites for OH⁻, accelerating the constant-rate step of dehydrogenation of 5-hydroxy-methyl-2-furanocarboxylic acid (HMFCA) intermediates [19]. Further to oxygen vacancies, the cationic vacancies also play an important role in enhancing the HMFOR activity due to their unique electron property and orbital distribution. However, the large formation energy of cationic vacancies makes them more difficult to fabricate and deeper to recognize. More importantly, under such harsh synthesis conditions, most of the cationic vacancies are generated in the bulk phase, which could not be fully utilized in catalytic interface. Therefore, it is a key to find a simple and effective strategy to control or selectively construct the surface cationic vacancy defects, and then systematic studying the structure-activity relationships between cationic vacancy and electrocatalytic HMFOR ability.

Herein, we fabricated vacancy-enriched V_{Mo}-NiO_xH_y catalyst derived from Mo-doped Ni₃S₂ via a mild electrochemical selective cation removal strategy, and the maximizing exposed cationic Mo vacancy benefited for the formation of active species (Ni³⁺-O) for accelerating HMFOR kinetics. The amorphous precursor may lead to the unstable dispersion and precipitation of Mo ions on the surface of the Ni₃S₂ under the action of current polarization, resulting in the formation of surface vacancy during the in-situ oxidation process. The surface vacancy can be fully utilized to effectively regulate the oxidation and reduction reactions on the catalyst surface during the catalytic process. A series characterization results demonstrate the existence of cation vacancy from atomic structure and macroscopic level. In situ Raman results confirm that cation vacancies induce the formation of electron-deficient Ni³⁺-O species from Ni-OH. Further, density functional theory (DFT) results demonstrate that the vacancy defects reduce the free energy of Ni-OH dehydrogenation and promote pre-oxidation behavior from Ni²⁺-OH to real active Ni³⁺-O species. Specifically, the electro-generated high-valence Ni³⁺-O group contributes the non-electrochemical oxidation of HMF molecules, enhancing the intrinsic activity of HMFOR. Benefiting from the cation vacancy effect, the as-prepared V_{Mo}-NiO_xH_y exhibits an optimized HMFOR performance with a current density of 205 mA cm⁻² at 1.4 V vs. reversible hydrogen electrode (RHE), which is superior to pristine NiO_xH_y (1.4 V vs. RHE at 70 mA cm⁻²). Besides, the catalytic effect of cation vacancy promotes the biomass electro-oxidation on alcohol and furfural as well. By coupling with HER, the cell voltage required for the hybrid electrolyzer is 240 mV lower than that for the overall water splitting at 100 mA cm⁻². This work elucidates the pre-oxidation enhancement behavior of Mo cation vacancy defects and provides a new insight into constructing highly efficient catalyst for HMFOR.

2. Experimental Section

2.1. Preparation of Materials

Mo-Ni₃S₂ nanosheets were prepared by a two-step hydrothermal method. Firstly, Ni foam (NF, 3 cm × 4 cm) was pretreatment in a mixture solution of HCl and deionized water (volume ratio 1:3) under ultrasonication for 15 min to remove surface oxide layer, following by washing the NF with distilled water and ethanol several times until pH ≈ 7, respectively. In a typical synthesis, Ni(CH₃COOH)₂·4 H₂O (4 mmol), (NH₄)₆Mo₇O₂₄·4 H₂O (0.32 mmol, 0.64 mmol, 0.96 mmol), CO(NH₂)₂ (20 mmol) and NH₄Cl (8 mmol) were dissolved in 80 mL deionized water under stirring to form a transparent solution. Then, the obtained clear solution was transferred into a 100 mL Teflon-lined stainless autoclave and a piece of cleaned NF was immersed into the solution. The autoclave was sealed and maintained at 160 °C for 1.5 h in a blast drying oven to obtain the NiMo-precursor. The Mo doped Ni₃S₂ was prepared via a hydrothermal process. Typically, the as-prepared NiMo-precursor (2 cm × 3 cm) was immersed into the 50 mL Teflon autoclave vessel filled with a 0.02 M Na₂S·9 H₂O solution and heated to 150 °C for 6 h.

The obtained materials are denoted as Mo_x-Ni₃S₂ (x = 0.32, 0.64, 0.96). Unless otherwise stated, all the involved Mo-Ni₃S₂ in this work refers to Mo_{0.64}-Ni₃S₂. The preparation of Ni₃S₂ was similar to Mo-Ni₃S₂ except without the amounts of Mo resource. To make the catalyst surface evolve into V_{Mo}-NiO_xH_y, the Mo-Ni₃S₂ and the control sample Ni₃S₂ were pre-oxidized by cyclic voltammetry (CV) process in 1.0 M KOH with scan rate of 20 mV/s for 40 cycles.

2.2. Materials characterizations

The morphologies of the catalysts were characterized by field emission scanning electron microscopy (FE-SEM (JSM-7500, Japan) and transmission electron microscopy (TEM) and atomic-resolution high-angle annular dark-field scanning transmission electron microscopy (AC HAADF-STEM) images equipped with an energy-dispersive spectrometer (EDS) were performed on JEM-ARM 200 F with an accelerating voltage of 200 kV. The X-ray absorption fine structure data were collected at the BL14W1 station in the Shanghai Synchrotron Radiation Facility (SSRF). The X-ray absorption spectra (XAS) were collected on the beam line BL01C1 in NSRRC. The chemical composition and surface states were analyzed by X-ray diffraction (XRD, Rigaku D/max-2400) and X-ray photoelectron spectroscopy (XPS, PHI 5000), respectively. The electron paramagnetic resonance spectroscopy (EPR) were taken using a Bruker EMXnano.

2.3. Electrochemical measurements

All electrochemical measurements were conducted on a CHI 760E (Chenhua) electrochemical workstation in a standard three-electrode system at room temperature, where the as-prepared catalyst (1 × 1 cm²), carbon rod and Hg/HgO were used as work electrode, counter electrode, and reference electrode, respectively. All the electrochemical tests with HMF were carried out with continuous stirring. The presented potentials in this work were converted into reversible hydrogen electrode (RHE) according to the Nernst equation: $E_{(RHE)} = E_{(Hg/HgO)} + 0.059 \text{ pH} + 0.098$. The linear sweep voltammetry (LSV) curves for HMF oxidation were collected in an undivided cell with the scan rate of 5 mV/s in electrolyte of 1 M KOH with 10 mM HMF. 90% iR-compensation was applied to correct the ohmic potential drop caused by the solution resistance. Chronoamperometry was carried out at potential of 1.35 V within 10 mL 50 mM HMF (the theoretical charge demand for full conversion is ~289 C). The constant potential electrolysis was conducted in a H-type electrolytic cell that are separated by a proton exchange membrane (Nafion 117), where the electrooxidation of HMF occurred on the as-prepared catalyst in the anodic chamber. Unless otherwise stated, all of the above electrochemical tests were performed under continuous agitation. For the two-electrode electrolyzer, both cathode and anode were V_{Mo}-NiO_xH_y.

2.4. In situ Raman spectrum tests

In situ Raman spectrum was carried out on the confocal Raman microscope (Alpha300R, WITEC, Germany 532 nm laser) under different potentials by CHI 760E electrochemical workstation. The electrolytic cell for in situ Raman spectroscopy includes a Teflon shell, a quartz glass plate, and a glassy carbon electrode. A semiconductor laser with a wavelength of 532 nm was used as the excitation light source. It was focused by 50-times long focal lens to vertically illuminate. All the electrochemical tests were carried out with the three-electrode configuration. It was coated with the as-prepared catalyst and served as the working electrode. A SCE electrode served as reference electrode and a Pt wire served as counter electrode. The SCE reference electrode was corrected by testing the RHE potential with a platinum gauze electrode in 1 M KOH hydrogen-saturated solution. For the HMFOR system, electrolyte is 1 M KOH with 0.5 M HMF.

2.5. Computational methods

The density functional theory (DFT) calculations to calculate the dehydrogenation free energy were implemented using the Vienna ab initio simulation package (VASP), using Perdew-Burke-Ernzerhof (PBE) flavor of DFT [20,21] and the projector augmented wave (PAW) method to account for the interactions between core and valence electrons [22, 23]. The kinetic energy cutoff for plane-wave basis was set to 400 eV cutoff was used for describing valence electrons. The van der Waals (vdW) interactions among HMF molecular and surfaces of β -Ni(OH)₂ with or without cation vacancies were calculated by the DFT-D3 method. Ni(OH)₂ is a (4 × 4) supercell of the (001) surface. The force convergence criterion was set to -0.05 eV/Å and energy convergence criterion was 10^{-5} eV. Brillouin-zone integrations were performed on Monkhorst-Pack gamma centered mesh. The k-point grids were $2 \times 2 \times 1$ for V_{Mo}-Ni(OH)₂, Ni(OH)₂ supercells. A vacuum layer of 15 Å was adopted in the three models.

The DFT calculations [24,25] to explore the cation vacancy effect on HMF adsorption were carried out in the CP2K code [26]. All calculations employed a mixed Gaussian and planewave basis sets. Core electrons were represented with norm-conserving Goedecker-Teter-Hutter pseudopotentials [27–29], and the valence electron wavefunction was expanded in a double-zeta basis set with polarization functions [30] along with an auxiliary plane wave basis set with an energy cutoff of 360 eV. The generalized gradient approximation exchange-correlation functional of Perdew, Burke, and Enzerhof (PBE) [31] was used. Each configuration was optimized with the Broyden-Fletcher-Goldfarb-Shanno (BFGS) algorithm with SCF convergence criteria of 1.0×10^{-6} au. The van der Waals correction of Grimme's DFT-D3 model was also adopted [32].

The adsorption energy of HMF were calculated by the following equation:

$$\Delta E = E(\text{HMF} - \text{adsorbent}) - E(\text{adsorbent}) - E(\text{HMF})$$

Where E(HMF-adsorbent), E(adsorbent), E(HMF) denote the energies of HMF-Ni(OH)₂ or HMF-V_{Mo}-Ni(OH)₂ complex, the Ni(OH)₂ or V_{Mo}-Ni(OH)₂, and HMF, respectively.

2.6. Determination of the Products

For quantitative analysis of products, High performance liquid chromatography (HPLC, Shimadzu Prominence LC-2030 C system, Japan) with an ultraviolet visible detector was used to analyze HMF oxidation products. The mobile phase A was methanol, and phase B was 5 mM ammonium formate aqueous solution, the volume ratio of A:B is 3:7, the flow rate is 0.6 mL min⁻¹. For each analysis, 20 μ L of the electrolyte after the potentiostatic electrolysis process was diluted to 2 mL with ultra-pure water. Using a 4.6 mm × 150 mm Shim-pack GWS 5 μ m C18 column, each separation lasts 10 min.

HMF and oxidation products were quantitatively determined based on the calibration curves of those standard solutions. The performance metric parameters involving, HMF conversion, product yield, FDCA selectivity and Faradaic efficiency (FE) for the electrocatalytic oxidation of HMF were calculated by the following equations:

$$\text{HMF conversion}(\%) = \frac{n(\text{HMF consumed})}{n(\text{HMF initial})} \times 100\% \quad (1)$$

$$\text{Product yield}(\%) = \frac{n(\text{product formed})}{n(\text{HMF initial})} \times 100\% \quad (2)$$

$$\text{FDCA selectivity}(\%) = \frac{n(\text{FDCA formed})}{n(\text{total oxidative products})} \times 100\% \quad (3)$$

$$\text{FE}(\%) = \frac{6 \cdot F \cdot n(\text{FDCA formed})}{\text{total charge passed} \cdot (C)} \times 100\% \quad (4)$$

where F is the Faraday constant (96485 C mol⁻¹).

3. Results and discussion

3.1. Synthesis and structure characterization of Mo doped Ni₃S₂

As depicted in Fig. 1a, the proof-of-concept model catalyst Mo doped Ni₃S₂ (Mo-Ni₃S₂) nanosheets was fabricated via a two-step hydrothermal method. The NiMo-precursor with porous network structure was first synthesized and then the target catalyst was obtained via hydrothermal vulcanization. The crystal structure of Ni₃S₂ and Mo-Ni₃S₂ was characterized by X-ray diffraction (XRD). As shown in Fig. 1b, compared to Ni₃S₂ (PDF#44-1418), the diffraction peaks of the Mo-Ni₃S₂ show a slight shift to lower angles, indicating successful implantation of Mo that renders lattice parameter expansion due to its larger atomic radius (Fig. 1b and Fig. S1).

To identify the surface valence states and variation in electronic structures before and after Mo doping, X-ray photoelectron spectroscopy (XPS) was carried out. In addition to the co-existence of Ni and S elements, Mo-Ni₃S₂ presents Mo signals, indicating successful Mo doping (Fig. S2a). Compared with pristine Ni₃S₂, the Ni 2p XPS spectra of Mo-Ni₃S₂ exhibits a positive-shift of ~ 0.3 eV and the relative ratio of (Ni⁰ + Ni²⁺)/Ni³⁺ is remarkably decreased (Fig. 1c, and Table S1), indicating that the average valence state of the Ni species in Mo-Ni₃S₂ is increased with the implantation of Mo atoms. Accordingly, an electron-transfer process is speculated to take place where Mo is the electron acceptor [33]. Another peak located at 852.7 eV is well matched with Ni 2p signal derived from Ni⁰ [34]. As for Ni₃S₂, the two peaks located at 161.4 and 162.3 eV can be attributed to S 2p_{3/2} and S 2p_{1/2} orbitals, respectively [35]. It should be noted that with Mo doping, the binding energies of S 2p in Mo-Ni₃S₂ slightly shifted ~ 0.3 eV positively compared with that of Ni₃S₂, suggesting the lower electronic density around the S atoms after Mo doping (Fig. S2b). With respect to the Mo 3d spectra (Fig. 1d) which overlaps the S 2 s transition (226.0 eV), suggesting the formation of Ni-S and Mo-S bindings [36,37]. The XPS signals are deconvoluted into two core levels of Mo 3d_{3/2} (232.2 eV) and Mo 3d 3d_{5/2} (228.6 eV) demonstrating the existence of Mo⁴⁺ [38].

Scanning electron microscopy (SEM) and transmission electron microscopy (TEM) were employed to observe the microstructure variation of the samples. The SEM and TEM images show that pure Ni₃S₂ exhibits cross-linked nanosheet arrays (Fig. S3a–c). Corresponding high-resolution TEM images (HR-TEM), selective area electron diffraction (SAED) patterns and energy dispersive X-ray spectroscopy (EDX) images demonstrate further reveal successful preparation of Ni₃S₂ (Fig. S3). After modification with Mo, the morphology changes from the micro-flower shape self-assembly tiny nanosheets to the micro-column structure (Figs. 1e and S4–5). From the aberration-corrected high-angle annular dark-field scanning transmission electron microscopy (AC HADDF-STEM) images and profiles inside the regular areas of Mo-Ni₃S₂, clear lattice fringes with a spacing of 0.28 nm can be seen (Fig. 1f–g), which belongs to the (110) crystal plane of hexagonal Ni₃S₂, further proving the unaltered crystal structure of Mo-Ni₃S₂. EDX elemental mapping images demonstrate the coexistence and uniform distribution of Mo, Ni, and S elements in Mo-Ni₃S₂ nanosheets (Fig. 1h), which is consistent with the above results, illustrating the introduction of Mo in the Mo-Ni₃S₂ catalyst.

3.2. The structural evolution and characterization of V_{Mo}-NiO_xH_y

It is widely accepted that transition metal sulfides serve as pre-catalyst for anodic electrooxidation reactions, and the real active species is metal hydroxides or oxides (MO_xH_y) generated from structural reconstruction due to the structural instability of metal sulfides under oxidative conditions [39,40]. Therefore, the proof-of-concept model catalyst Mo-Ni₃S₂ and the control sample Ni₃S₂ were pre-oxidized by

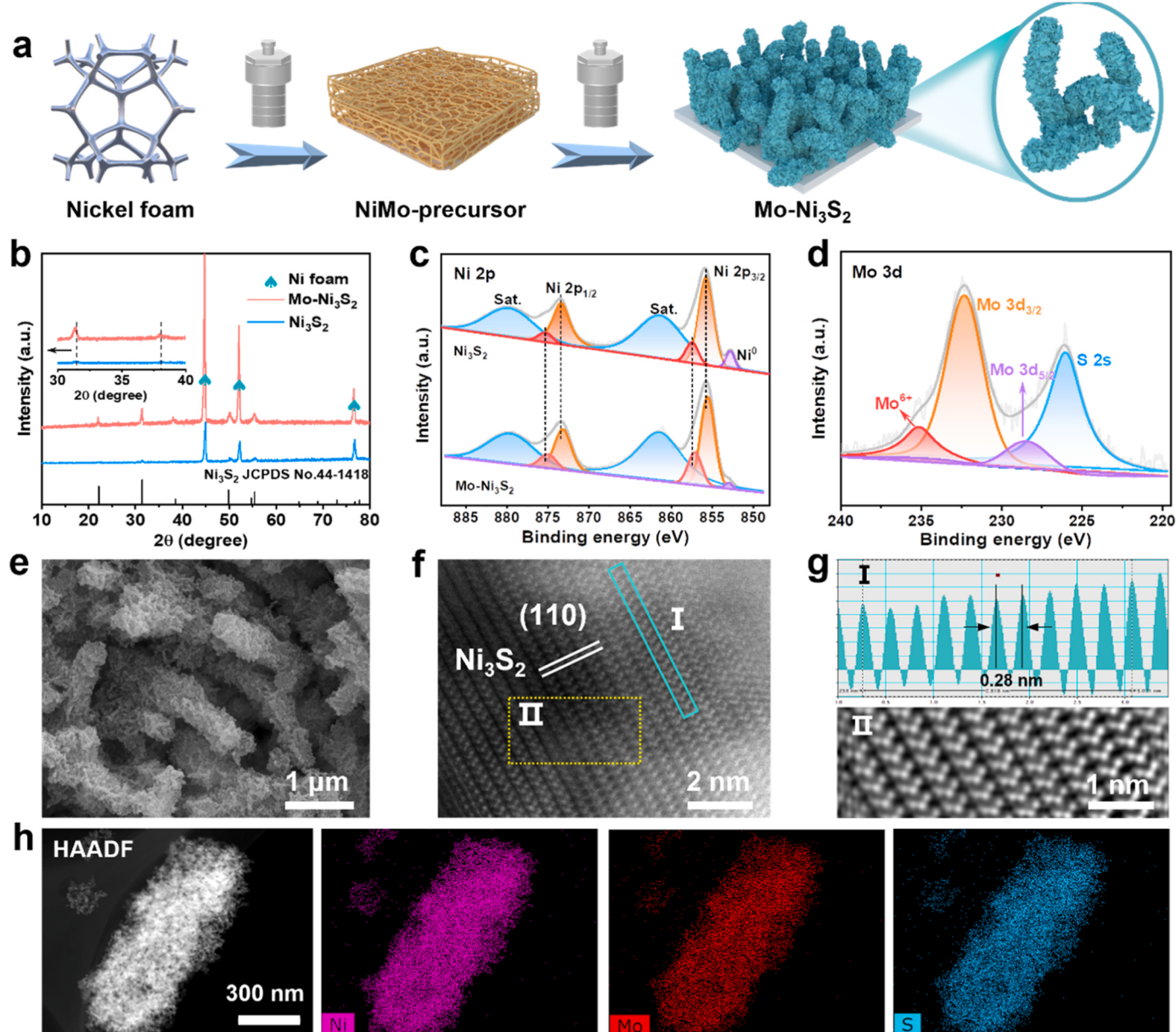


Fig. 1. (a) Scheme of the synthesis process for Mo-Ni₃S₂. (b) XRD patterns of Ni₃S₂ and Mo-Ni₃S₂. (c) XPS Ni 2p spectra of Ni₃S₂ and Mo-Ni₃S₂. (d) XPS Mo 3d spectra of the Mo-Ni₃S₂. (e) SEM images of Mo-Ni₃S₂. (f) HAADF-STEM, (g) Intensity profile (I) recorded and IFFT patterns (II) of corresponding areas in Fig. 1f and (h) EDX-STEM elemental mapping images of Mo-Ni₃S₂.

cyclic voltammetry (CV) process in 1.0 M KOH (Fig. 2a and S6). Mo-Ni₃S₂ exhibits a superior oxidation current than that of Ni₃S₂, suggesting the introduction of Mo promotes the oxidation (Fig. S6). Nevertheless, its specific configuration and role of specific oxidation in regulating the catalyst structure remains ambiguous. Therefore, the scheme of possible electrocatalyst evolution is proposed and shown in Fig. 2b. Specifically, as the potential increases, Ni²⁺ is pre-oxidized to Ni^{2+δ} and Ni₃S₂ undergoes structural reconstruction into nickel hydroxides or oxides (denoted as NiO_xH_y) by electrooxidation. This phenomenon can be attributed to the detachment of sulfur anions from Ni₃S₂ during repeated reoxidation and reduction processes. These sulfur anions then react with OH⁻ and air in the solution, leading to the formation of oxygen anions (such as sulfate ions of SO₄²⁻) [41,42]. As the anions undergo oxidation and dissolution, the transition metal site will react with OH⁻ to form metal-based (oxy)hydroxides. Various factors contribute to the formation of molybdenum defects, including the presence of acidic MoO_x in amorphous NiMo-precursor with fluffy

porous nanonetworks (Fig. S7), which is widely recognized with high tendency to dissolve in strong alkaline solution. In conjunction with the XPS results of Mo 3d (Fig. 1d), it can be inferred that amorphous molybdenum sulfide could exist on the surface of nickel sulfide. During the CV cycles, when the catalyst surface is at a high potential, molybdenum ions will be dissolved from the surface into the solution. Also, the long-range disorder of amorphous precursors and molybdenum sulfide leads to a large number of suspension bonds on the surface [43], which may lead to unstable Mo ions dispersion on the catalyst surface and exsolution. Consequently, under the effect of applied oxidative voltage, the process of activation and pre-oxidation will lead to the in situ anodic leaching of Mo in Mo-Ni₃S₂ and the final catalyst evolves into nickel hydroxide with Mo cationic vacancy (denoted as V_{Mo}-NiO_xH_y).

The presence of cation vacancy could profoundly affect the properties of catalyst yet a direct observation remains challenging [44]. To this end, we conducted multiple characterizations, including XPS, inductively coupled plasma-mass spectrometry (ICP-MS), AC HAADF-STEM,

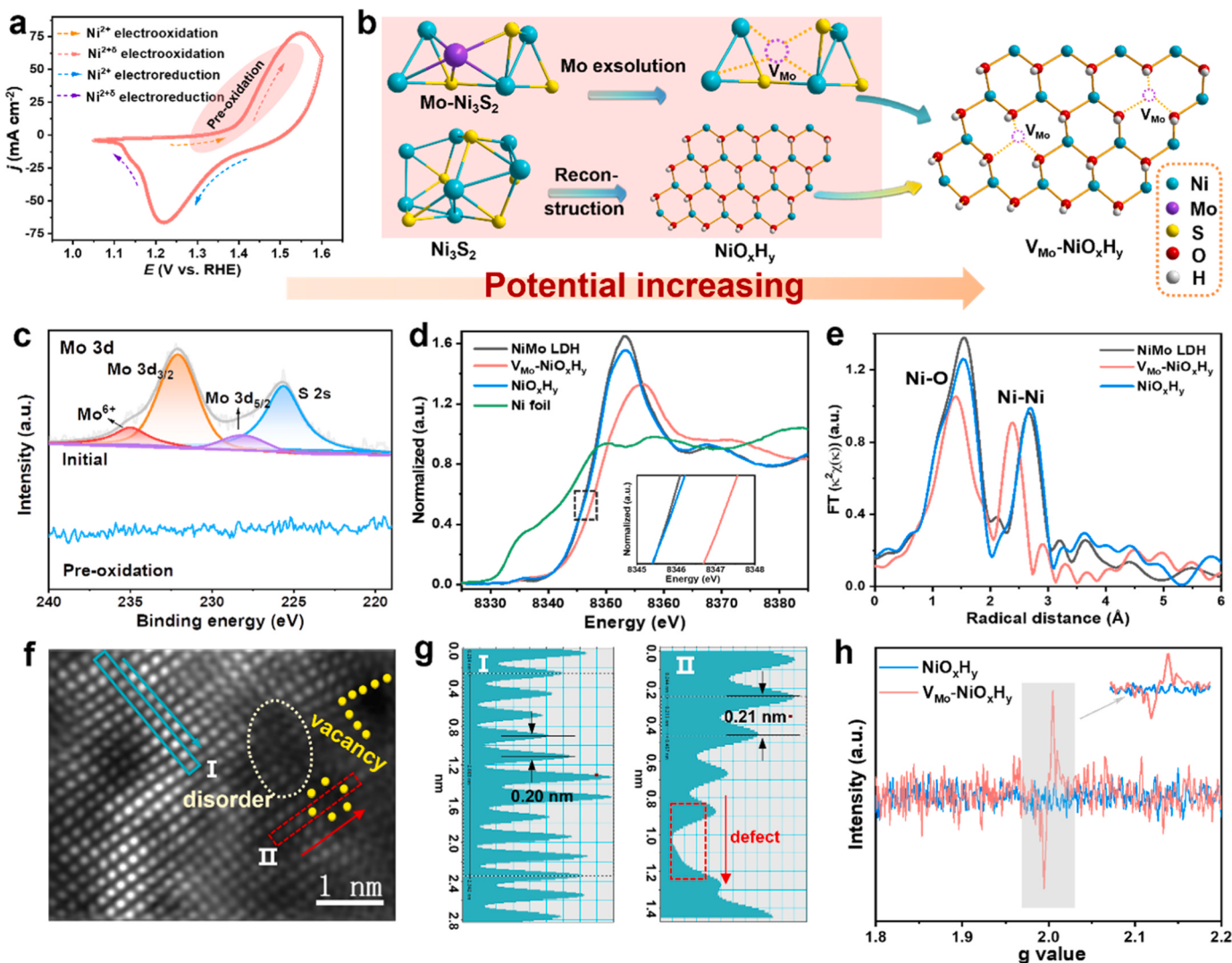


Fig. 2. (a) CV curve of fabricated Mo-Ni₃S₂. (b) The scheme of the relationship between electrocatalyst evolution and potential. (c) XPS spectra of Mo 3d of Mo-Ni₃S₂ before and after pre-oxidation. (d) Ni K-edge XANES spectra. Inset, the magnified pre-edge XANES region. (e) Fourier-transformed EXAFS spectra at Ni K-edge for V_{Mo}-NiO_xH_y, NiO_xH_y, the reference NiMo LDH and Ni foil. (f) AC HAADF-STEM image of V_{Mo}-NiO_xH_y. (g) Profiles inside the rectangular area of the HADDF-STEM image in 2 f (I comes from blue-green profile, II comes from red profile). (h) EPR spectra of V_{Mo}-NiO_xH_y and NiO_xH_y.

and electron paramagnetic resonance (EPR) to investigate the atomic and electronic structures, and unveil the structural evolution of the catalyst. According to the full XPS spectra of catalyst (Fig. S8), Mo and S elements were not detected after the pre-oxidation process, suggesting electrogenerated reconstitution occurs on the surface of the catalyst. According to the Ni 2p XPS spectrum, the peak of the V_{Mo}-NiO_xH_y catalyst exhibits a slight positive shift compared with that of the pristine Mo-Ni₃S₂ pre-catalyst (Fig. S9). The Ni-S and Mo-S bonds almost disappear after CV activation (Fig. S10), suggesting that the surface of Mo-Ni₃S₂ may evolve to V_{Mo}-NiO_xH_y as the actual active electrocatalyst. TEM-EDX analysis revealed the absence of molybdenum species on the material surface following cyclic voltammetry activation, and the sulfur concentration was determined to be below 0.5% (Table S2 and Table S3). Meanwhile, the ICP results demonstrate that the Mo cation and S anion concentrations in the electrolyte change from negative to positive after pre-oxidation, suggesting Mo and S leaching from catalyst to electrolyte (Fig. S11 and Table S4). The above results laterally validate the conjectures of catalyst structure evolution and vacancy formation.

Furthermore, X-ray absorption spectroscopy (XAS) was applied to investigate the valence state and local coordination environment of V_{Mo}-

NiO_xH_y. The Ni K-edge spectra of the NiO_xH_y and NiMo LDH samples are similar (Fig. 2d). Notably, positively energy shift of the V_{Mo}-NiO_xH_y in the amplified spectral features indicates increased average valence state (inset Fig. 2d), indicating an increased oxidation state of Ni to compensate for the charges of the etch Mo cations. From Fourier-transformed (FT) of the extended X-ray adsorption fine structure (EXAFS) oscillations region, structural deviation can be observed between V_{Mo}-NiO_xH_y and conference samples (Fig. S12). This suggests the difference in coordination surrounding the centered metal atoms of V_{Mo}-NiO_xH_y. In the FT R-space (Fig. 2e), NiMo LDH, NiO_xH_y present similar Ni coordinative geometry with two main peaks of Ni-O at about 1.62 Å and Ni-Ni at around 2.75 Å [45]. In V_{Mo}-NiO_xH_y, however, the intensity of both peaks decreases (Fig. 2e), indicating that more Ni cations transition to an unsaturated coordination state [46]. Notably, the strength of the Ni-Ni peaks is lower than that of NiO_xH_y, indicating a reduced coordination number (CN) and the existence of Mo defect. Moreover, the disorder region and cationic Mo vacancies can be observed in the atomic-scale HAADF-STEM image and the inverse fast Fourier transform (IFFT) images marked with yellow boundary (Fig. 2f and S13). The profiles of rectangular areas inside Fig. 2f shows lattice fringes with spacing of 0.20 nm and 0.21 nm assigned to (210) and (103) crystal

planes of NiOOH and Ni(OH)₂ (Fig. 2g), respectively. The intensity profiles (Fig. 2g) of the framed regions in Fig. 2f verify the vacancy nature of V_{Mo}-NiO_xH_y. Further, EPR was used to investigate the existence of vacancy. Generally, vacancies induce the formation of paramagnetic species with asymmetric electrons that are highly sensitive with EPR [47]. The EPR spectrum of V_{Mo}-NiO_xH_y shows a strong electron paramagnetic resonance intensity at $g = 2.003$, while no EPR signal of V_{Mo} is observed in pristine NiO_xH_y (Fig. 2h), proving the formation of cationic V_{Mo} defects and no sulfur vacancy was formed during the reconstruction process [48,49]. The advanced atomic characterization and EPR results directly confirm the creation of cationic vacancies.

3.3. Electrocatalytic performance

As a proof of concept, we applied V_{Mo}-NiO_xH_y grown on nickel foam as a self-supported electrode for electrocatalytic HMFOR (Fig. S14). The V_{Mo}-NiO_xH_y exhibits a potential of 1.36 V vs. RHE at a current density of 100 mA cm⁻² for HMF oxidation, which is much lower than that of V_{Mo}-NiO_xH_y for OER (Fig. 3a). Moreover, V_{Mo}-NiO_xH_y displays superior

catalytic performance (1.4 V vs. RHE at 205 mA cm⁻²) to pristine NiO_xH_y (1.4 V vs. RHE at 74 mA cm⁻²) for HMFOR (Figs. 3a and 3c), which is comparable to most of the electrocatalysts reported so far, as shown in Table S5. In addition, V_{Mo}-NiO_xH_y exhibits lower Tafel slope for HMFOR (32 mV dec⁻¹) and OER (118 mV dec⁻¹) than that of NiO_xH_y (84 and 121 mV dec⁻¹, respectively), indicating the dramatically enhanced kinetics towards HMF electrooxidation due to the formation of Mo vacancy (Fig. 3b). Meanwhile, the Tafel slopes of the HMF oxidation are lower than those of OER processes, manifesting easier electron transfer between the interfaces of HMF and catalyst. The Nyquist plot of V_{Mo}-NiO_xH_y exhibits a smallest diameter semicircle (Fig. S15), suggesting faster charge transfer could be attained on catalyst surface, contributing to promoted HMFOR activity. To investigate the origin of the excellent electrocatalytic HMFOR activity of V_{Mo}-NiO_xH_y, the double-layer capacitance (C_{dl}) was evaluated by CV curves to eliminate the influence of electrochemically active surface area (ECSA) considering the proportional relationship between ECSA and C_{dl} (ECSA = C_{dl}/C_s , where C_s is the specific capacitance of the sample, $C_s = 0.040$ mF cm⁻² in 1.0 M KOH (Fig. S16) [50]. As presented in Fig. S16c, the

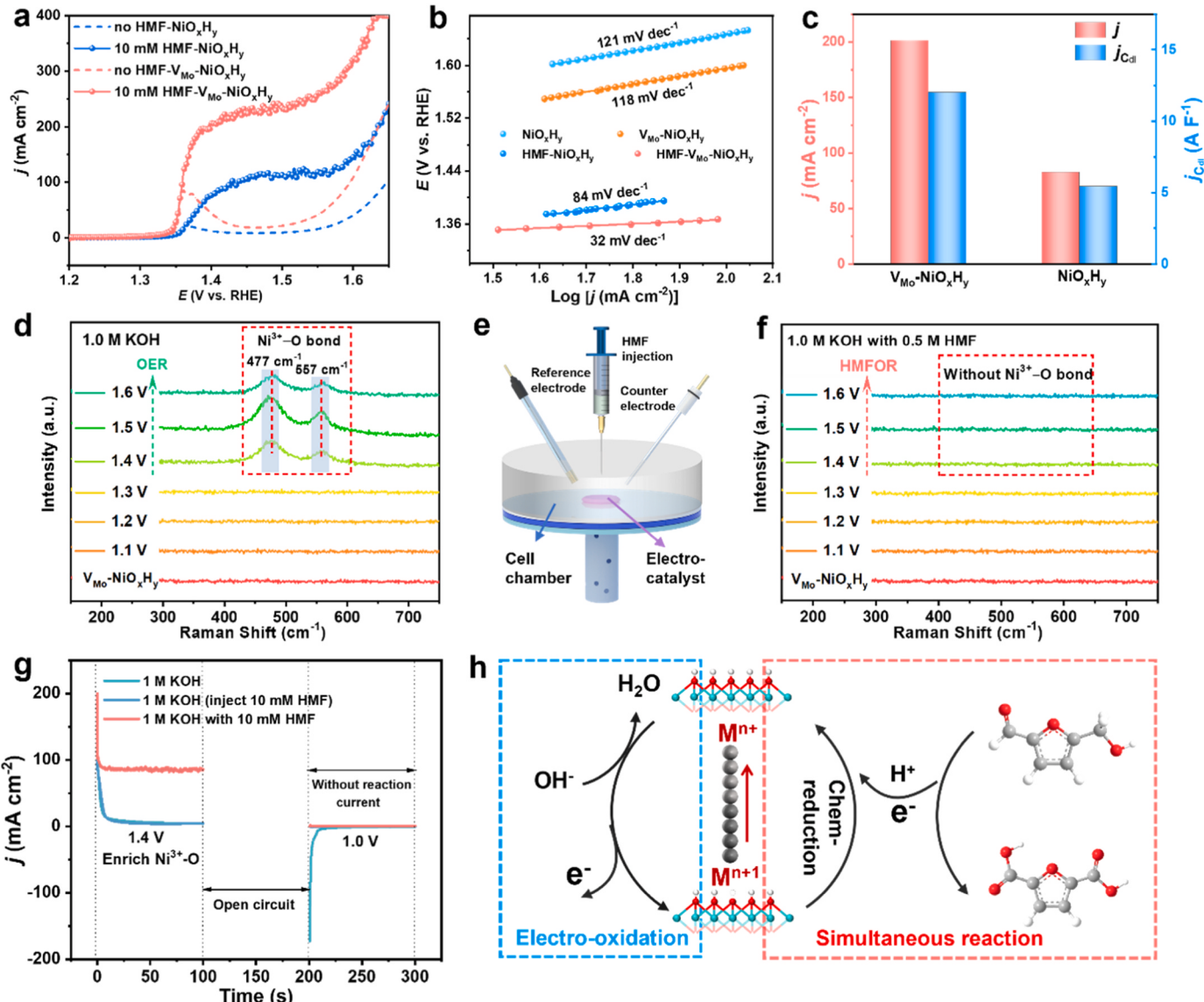


Fig. 3. (a) LSV curves and (b) Tafel plots of NiO_xH_y and V_{Mo}-NiO_xH_y in 1.0 M KOH with and without 10 mM HMF. (c) Corresponding current density and current density normalized by ECSA at 1.4 V vs. RHE for HMFOR. (d) in situ Raman spectra for V_{Mo}-NiO_xH_y electrode in 1.0 M KOH and (f) in 1.0 M KOH with 0.5 M HMF. (e) Schematic diagram for in situ Raman spectroscopy during electrochemical measurements. (g) Multi-potential step curves of the HMFOR over the V_{Mo}-NiO_xH_y electrode at 1.4 V. (h) The HMFOR mechanism schemes for V_{Mo}-NiO_xH_y.

calculated C_{dl} value of $V_{Mo}\text{-NiO}_x\text{H}_y$ is comparable with NiO_xH_y , indicating the introduction of Mo vacancy has contributed little to ECSA. Logically, the current density normalized by C_{dl} at 1.4 V vs. RHE of $V_{Mo}\text{-NiO}_x\text{H}_y$ is superior to pristine NiO_xH_y (Fig. S16d), suggesting the vacancies formed by molybdenum exsolution can promote the intrinsic activity of $V_{Mo}\text{-NiO}_x\text{H}_y$.

In situ Raman spectra were further conducted to investigate the reaction mechanism of HMFOR over $V_{Mo}\text{-NiO}_x\text{H}_y$. (Fig. 3d-f). As for OER process, two characteristic peaks at 477 and 557 cm^{-1} are observed at 1.4 V (Fig. 3d), which are assigned to the E_g bending and A_{1g} stretching vibrations of $\text{Ni}^{3+}\text{-O}$ generated from NiO_xH_y dehydrogenates [51,52], indicating the accumulation of Ni^{3+} species after 1.4 V. Differently, no peaks ascribed to $\text{Ni}^{3+}\text{-O}$ can be detected during the HMFOR process (Fig. 3f). According to previous literatures, NiO_xH_y will reconstruct to $\text{NiO}_x\text{H}_{y-1}$ and then participate in HMF oxidation with continuous phase transition process ($\text{NiO}_x\text{H}_y \rightarrow \text{NiO}_x\text{H}_{y-1} \rightarrow \text{NiO}_x\text{H}_y$) [53,54]. It is reasonable to assume that the $\text{NiO}_x\text{H}_{y-1}$ obtained from the electrochemical oxidation process can spontaneously grab protons from HMF to form NiO_xH_y . Namely, the electrogenerated high-valence Ni^{3+} species will be rapidly consumed and converted to Ni^{2+} by chemical reduction ("electrochemical-chemical", E-C mechanism), accompanied by HMF oxidation to intermediates (electro-independent) that prevents the Ni^{3+} species accumulation. Therefore, no signal of $\text{Ni}^{3+}\text{-O}$ can be observed during the whole potential range of HMFOR. To further analyze the influence of water oxidation to HMFOR, the CV measurements were conducted, and the results are shown in Fig. S17. In 1 M KOH with 10 mM HMF solution, only one oxidation peak attributed to Ni^{2+} oxidation can be observed in the range of 0.8–1.4 V (Fig. S17a-b). And the negative sweep current is slightly greater than that of oxidation current at ranges of 1.6 to 1.3 V, which may be ascribed to that the rate of reduction is not limited by substance diffusion and there are enough active species. When tested in 1 M KOH with 50 mM HMF, Fig. S17c-d illustrates that within the OH^* adsorption region (0.8 V–1.1 V), which corresponds to the oxidation of OH^- to OH^* ($\text{OH} \rightarrow \text{OH}^* + \text{e}^-$) [10,55], a weak oxidation current is observed. In the OH^* generation process region attributed to water dissociation ($\text{H}_2\text{O} \rightarrow \text{OH}^* + \text{H}^+ + \text{e}^-$) [56,57], no corresponding broad peaks centered at 1.36 V can be observed whether in 1 M KOH with 10 or 50 mM HMF, indicating negligible impact of the OH^* produced by water dissociation on HMFOR in a strong alkali environment. Additionally, preceding the electrooxidation of Ni^{2+} , no significant HMF oxidation current is noticeable, suggesting that the active substance of HMFOR on $V_{Mo}\text{-NiO}_x\text{H}_y$ might not be OH^* , but rather the electrogenerated Ni^{3+} . Furthermore, no reduction peak can be observed in Fig. S17c-d, indicating that Ni^{3+} produced by electro-oxidation participated in spontaneous oxidation of HMF. More critically, the voltage of Ni^{2+} electrooxidation to Ni^{3+} coincides with that of HMFOR (Fig. 3a and Fig. S17), implying that the primary active material of HMFOR on $V_{Mo}\text{-NiO}_x\text{H}_y$ is the high-valanced nickel species produced by Ni^{2+} electrooxidation.

The indirect oxidation mechanism was further investigated by the measurement of the multi-potential step curves. The change in active species reflects the variations in the electrode. As shown in Fig. 3g, at ranges from 0 to 100 s, high-valence $\text{Ni}^{3+}\text{-O}$ species were enriched through electrochemical oxidation of $V_{Mo}\text{-NiO}_x\text{H}_y$ at 1.4 V vs. RHE. Then the potential was switched to the open circuit potential (OCP). At 200 s, an electroreduction-related current from the high-valent species transition to pristine species could be observed at 1.0 V vs. RHE under OER conditions (1 M KOH), indicating that the accumulated high-valence nickel species can stably exist at OCP process, and then return to the initial state of the catalyst through electroreduction in 200–300 s. On the contrary, after injected HMF, the signal of reduction current disappeared. Furthermore, when HMF was injected before test (1 M KOH with 10 mM HMF) for HMFOR tests, a higher anodic current could be observed, indicating the occurrence of HMFOR. Uniformly, no obvious reduction current signal can be observed during the 1.0 V test (200–300 s), demonstrating that the reaction between the accumulative

$\text{Ni}^{3+}\text{-O}$ species and HMF is spontaneous, which is consistent with the in situ Raman results. Based on the above outcomes, we propose that the HMFOR over $V_{Mo}\text{-NiO}_x\text{H}_y$ is dominated by E-C mechanism. Hence, we believe that HMFOR involves two continuous single-electron transfer processes. First, under the power of electricity, the reconstructed $\text{Ni}^{2+}\text{-O}_x\text{H}_y$ is oxidized to $\text{Ni}^{3+}\text{-O}_x\text{H}_{y-1}$ by losing a proton to react with OH^- . Simultaneously, $\text{Ni}^{3+}\text{-O}_x\text{H}_{y-1}$ spontaneously and rapidly grabs protons and electrons from HMF, resulting in chemically reverting to $\text{Ni}^{2+}\text{-O}_x\text{H}_y$ and electrocatalytic HMFOR (Fig. 3h). It should be pointed out that electro-oxidation of HMF in 1.0 M KOH is supposed to initiated following the formation of activated alcohol motif following the reaction of base with aldehyde group that without alpha active hydrogen (Cannizzaro-type reaction) [58]. Afterwards the deprotonation oxidation of alcohol motif is then mediated by $\text{Ni}^{2+}/\text{Ni}^{3+}$ redox couple.

To further investigated the electrochemical behavior of reaction interface during oxidation process, in situ electrochemical impedance spectroscopy (in situ EIS) was conducted [59]. The Nyquist plots of $V_{Mo}\text{-NiO}_x\text{H}_y$ at various voltages in 1.0 M KOH with and without HMF were compared. At the voltage of 1.1–1.4 V in OER process, the steep lines indicate the large resistance of the interfacial charge transfer (R_{ct}), suggesting weak interfacial reactivity [60]. When the voltage is higher than 1.45 V, the Nyquist plot exhibits a semicircle, manifesting the OER process occurs (Fig. S17a). Compared with the Nyquist plots in 1.0 M KOH, the Nyquist plots in 1.0 M KOH with HMF shows a semicircle at a low voltage of 1.35 V (Fig. S17b), which in accordance with oxidation position in LSV curves in Fig. 3a, indicating strong charge transfer between the electrode and the reaction interface and revealing the oxidation of HMF cases. The corresponding Bode phase plots are shown in Fig. S17c-d. As the potential increases from 1.5 to 1.6 V in 1.0 M KOH, the transition peak in the low-frequency region ($10^{-1}\text{--}10^1$ Hz) decreases significantly, corresponding to the decrease of R_{ct} , indicates faster interface charge transfer [59]. However, after injected HMF, an earlier peak occurs at 1.35 V and presents analogous decreases trend in the low-frequency region as well, mainly attributed to HMF oxidation. These results illustrate that the HMF oxidation possesses priority over OER process.

3.4. Density functional theory simulation and product analysis

DFT calculation was performed to give an insight into V_{Mo} on the dehydrogenation kinetics of $\text{Ni}^{2+}\text{-OH}$, corresponding to the detailed HMFOR mechanism. Based on the model of $\text{Ni}(\text{OH})_2$ (110) surface with Ni as the active site, the specific free energies of Ni-OH dehydrogenation step for $V_{Mo}\text{-NiO}_x\text{H}_y$ and NiO_xH_y are presented in Fig. 4a. Obviously, the dehydrogenation process on the surface of NiO_xH_y is energetically unfavorable (1.39 eV). In comparison, the free energy decreases significantly after introducing cation vacancy (0.79 eV), indicating that the vacancy is conducive to the dehydrogenation process. According to previous studies [61–63], the oxidation process of HMF for nickel-based catalyst involves the redox couple of $\text{Ni}^{2+}/\text{Ni}^{3+}$, including the electro-generated self-reconfiguration dehydrogenation of the catalyst ($\text{Ni}^{2+}\text{-OH} + \text{OH}^- \rightarrow \text{Ni}^{3+}\text{-O} + \text{H}_2\text{O} + \text{e}^-$) and the spontaneous proton-coupled electron transfer (PCET) process, which contains a chemical reduction of $\text{Ni}^{3+}\text{-O}$ to $\text{Ni}^{2+}\text{-HMF}$ dehydrogenation oxidation (Fig. 4b). In this process, electrooxidation of $\text{Ni}^{2+}\text{-OH}$ to $\text{Ni}^{3+}\text{-OH}$ is the rate determination step [62]. Specifically, the $\text{Ni}^{3+}\text{-O}$ species, serving as a chemical oxidant, react with HMF via non-electrochemical and rate-limiting hydrogen atom transfer (HAT). The high oxidation state $\text{Ni}^{3+}\text{-O}$ grabs proton and electron from the carbon at the alpha position of the geminal diol following the aldehyde oxidation path to the Ni^{3+} site in $\text{Ni}^{3+}\text{-O}$, thereby chemically reducing $\text{Ni}^{3+}\text{-O}$ to $\text{Ni}^{2+}\text{-OH}$ [64, 65]. The aforementioned results demonstrate that the introduction of V_{Mo} could significantly enhance the intrinsic activity of HMFOR by decreasing the free energy of NiO_xH_y dehydrogenation to the reactive mediator species, hence facilitates the thermodynamic behavior.

Further, DFT calculations revealed the adsorption free energy of

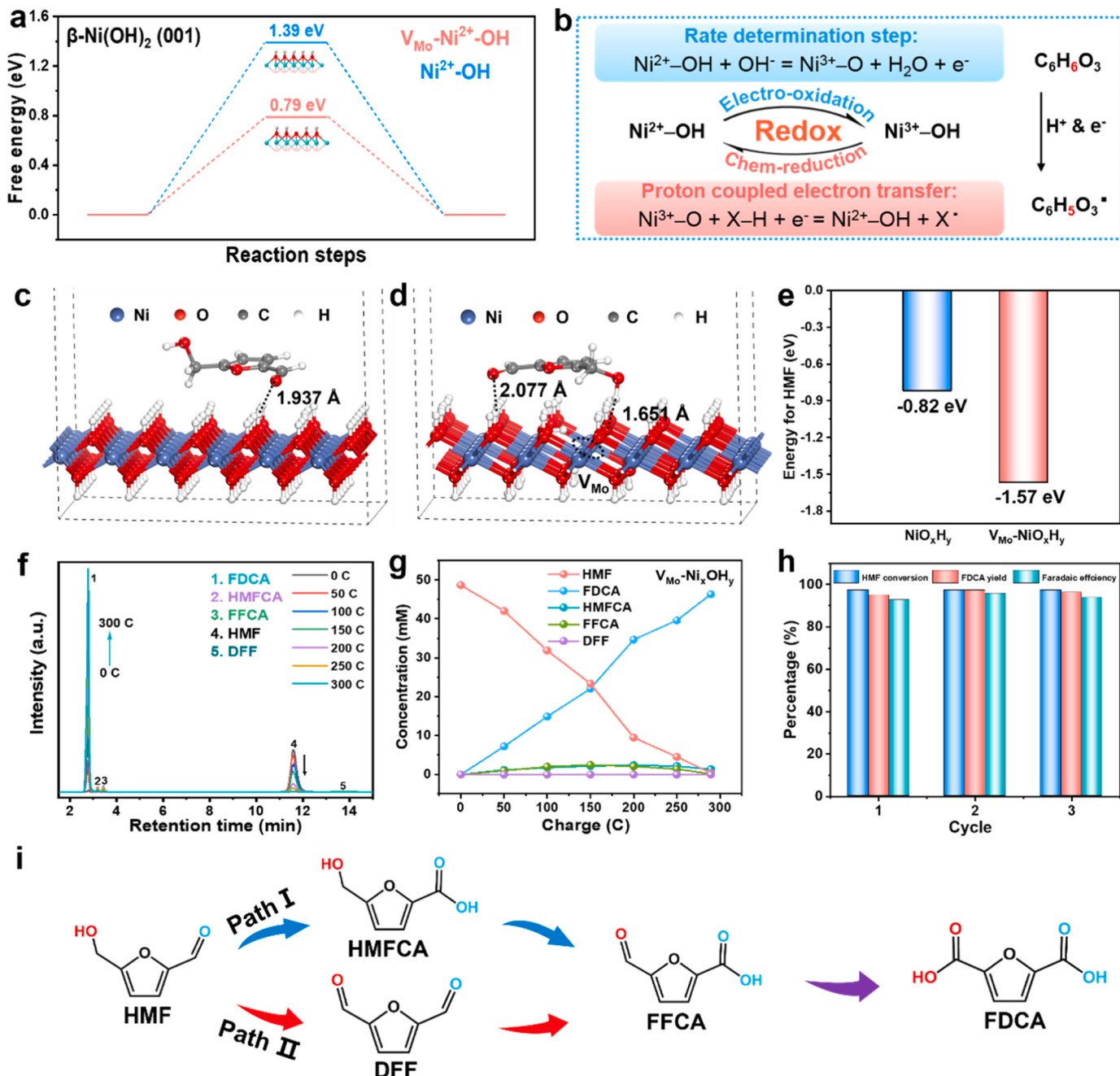


Fig. 4. (a) Free energies of Ni-OH dehydrogenation step for $\text{VMo-NiO}_x\text{H}_y$ and NiO_xH_y . (b) Schematic diagram for HMFOR mechanism including catalyst electro-generated and non-electrochemical step. Theoretical models of (c) NiO_xH_y , and (d) $\text{VMo-NiO}_x\text{H}_y$ adsorption HMF. (e) Adsorption free energy of HMF on $\text{VMo-NiO}_x\text{H}_y$ and NiO_xH_y . (f) The HPLC chromatogram traces and (g) concentration change curves of HMFOR. (h) The HMF conversion, FDCA yield and Faradaic efficiency of HMFOR over $\text{VMo-NiO}_x\text{H}_y$. (i) Possible reaction pathways for HMFOR.

HMF on NiO_xH_y and $\text{VMo-NiO}_x\text{H}_y$ surfaces. The adsorption models of HMF on NiO_xH_y (Fig. 4c) and $\text{VMo-NiO}_x\text{H}_y$ (Fig. 4d) were constructed. For NiO_xH_y , when HMF molecules are adsorbed on the surface, O on HMF forms a hydrogen bond with H on OH on the surface of NiO_xH_y , with the bond length of 1.937 Å. When adsorbed in the $\text{VMo-NiO}_x\text{H}_y$ structure, H of the OH at the vacancy will be oriented towards the vacancy, exposing O to form a strong hydrogen bond with H in the -OH on HMF molecule, with a bond length of 1.651 Å. Meanwhile, O on HMF and H on $\text{VMo-NiO}_x\text{H}_y$ surface form hydrogen bond of 2.077 Å. At this time, the adsorption energy was significantly enhanced. As can be seen from Fig. 4e, the adsorption energy of $\text{VMo-NiO}_x\text{H}_y$ catalyst for HMF (-1.82 eV) is much higher than that of NiO_xH_y (-1.57 eV), indicating

that cation vacancy can promote the kinetics of HMFOR.

To analyze the intermediates and products after chronoamperometric tests, high-performance liquid chromatography (HPLC) was performed to quantitatively calculate the concentration of HMF and as-generated products (Fig. 4f and S18). For HMF oxidation applying $\text{VMo-NiO}_x\text{H}_y$ as the electrocatalyst at 1.4 V (Fig. S19), HMF is almost 100% consumed when the charge quantity is 298 C (a theoretical charge) within a short time, suggesting a rapid conversion of HMF and a possibility to prevent the degradation of HMF under strong alkaline electrolyte. The relationship between the concentration of substances and the charge are depicted in Fig. 4g. The results show that the content of HMF decreases gradually along with charge increasing, while the

concentration of FDCA gradually increases as reaction proceed. In addition, the content of intermediate DFF is barely detectable, while the existence of both HMFCA and FFCA can be detected during the oxidation process, manifesting that HMF oxidation is likely following path I (HMFCA intermediate) to generate FDCA (Fig. 4i). It means that the aldehyde group is preferentially adsorbed on the surface of the catalyst and added with H_2O to form geminal diol under alkaline catalysis. Then, electrocatalytic dehydrogenation of the C–H bond and the O–H bond will be triggered under OH^- activation to form HMFCA intermediates. Besides, the catalyst retains a high FDCA yield (over 95%) and FE (about 93%) after three successive electrolysis cycles, indicating superior reactive stability for HMFOR of the $\text{V}_{\text{Mo}}\text{-NiO}_x\text{H}_y$ electrode (Fig. 4h). As shown in Fig. S20a, the sample still exhibits the characteristic peaks of Ni_3S_2 , and no new diffraction peaks appears, suggesting no apparent bulk crystal structure change after HMFOR. Further, the morphology of tiny nanosheets can be observed from the SEM and TEM images (Fig. S20b–d), indicating the catalyst maintained stable morphology. While after excessive oxidation in electrolyte with HMF (undergo OER process), the lattices of $\text{Ni}(\text{OH})_2$ and NiOOH can be identified, which indicates the catalyst surface converted to nickel (oxy)hydroxide after OER process (Fig. S20e–f), coinciding with results after CV activation in 1.0 M KOH.

3.5. Substrate expansion and couple reaction performances

To further display the superiority of cation vacancies, we finally evaluated the activities of $\text{V}_{\text{Mo}}\text{-NiO}_x\text{H}_y$ for furfuryl alcohol (single hydroxymethyl group on furan ring, R–OH) and furfural (single aldehyde group on furan ring, R–CHO) electrochemical oxidation. The $\text{V}_{\text{Mo}}\text{-NiO}_x\text{H}_y$ electrode exhibits a faster oxidation current rise than NiO_xH_y on R–OH and R–CHO (Fig. 5a and b), manifesting the cation vacancy has a universal effect on accelerating electrochemical biomass conversion. Moreover, the oxidation current densities of both NiO_xH_y and $\text{V}_{\text{Mo}}\text{-NiO}_x\text{H}_y$

NiO_xH_y on R–OH are higher than that of R–CHO (Fig. 5c), implying the oxidation of hydroxymethyl is the RDS of HMFOR and the introduction of V_{Mo} is an advanced strategy to accelerate the RDS rate and enhance the HMFOR kinetics [66].

The reduced onset potential and overpotential after replacing OER with HMFOR play an important role for enhancing energy utilization efficiency (Fig. 5d). When $\text{V}_{\text{Mo}}\text{-NiO}_x\text{H}_y$ was used as the anode and cathode catalyst for overall electrolysis of coupled reactions, as shown in Fig. 5e, after substituting OER for HMFOR, the hybrid cell electrolytic reaction presents lower cathodic potentials than that of water splitting, which is conducive to hydrogen production at a lower voltage. Besides, the overpotential to reach 100 mA cm^{-2} of hybrid cell on NiO_xH_y is 110 mV higher than that of $\text{V}_{\text{Mo}}\text{-NiO}_x\text{H}_y$ (Fig. S21), which proves that modification of cation vacancy evidently improves the performance of HMFOR&HER couple reactions.

4. Conclusions

A unique cation vacancy creation strategy was proposed to promote the production of active sites by cationic defects to improve the catalyst pre-oxidation process for efficient HMFOR. We reveal that in situ Mo and S leaching during the electrochemical activation process induces the cationic vacancy defects formation and surface reconstruction, which facilitates the generation of reactive electron-deficient $\text{Ni}^{3+}\text{-O}$ groups that propel the catalysis of HMF oxidation. The Mo cationic vacancy modulates the local configuration of the electron and reduces the dehydrogenation free energy of $\text{V}_{\text{Mo}}\text{-NiO}_x\text{H}_y$ to the reactive intermediates, thereby facilitating the pre-oxidation process of $\text{Ni}^{2+}\text{-OH}$ to active $\text{Ni}^{3+}\text{-O}$ species. Furthermore, the cationic vacancies promote the adsorption of HMF and contribute to the accessibility of the substrates to the active species. The as-generated $\text{Ni}^{3+}\text{-O}$ species squat towards grabbing rate-limiting H atoms and electrons from the alpha carbon of the geminal diol formed from aldehyde group addition with

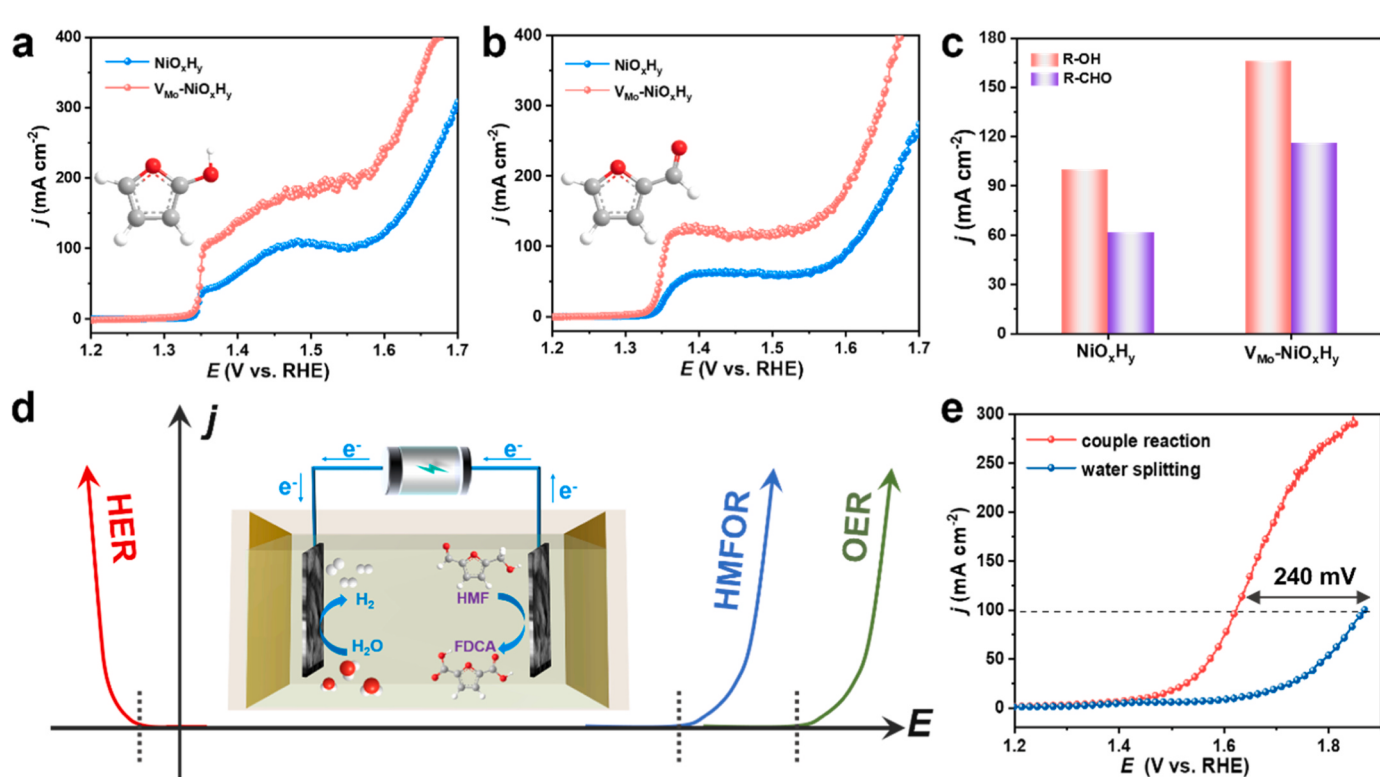


Fig. 5. (a) Electrochemical behavior of furfuryl alcohol (R–OH) oxidation and (b) furfural (R–CHO) oxidation on NiO_xH_y and $\text{V}_{\text{Mo}}\text{-NiO}_x\text{H}_y$. (c) The comparison of current density for R–OH and R–CHO oxidation at 1.45 V. (d) j – E curves and required potentials at the cathode and anode for electrolysis. (e) LSV curves for $\text{V}_{\text{Mo}}\text{-NiO}_x\text{H}_y$ couple in 1.0 M KOH with and without 10 mM HMF.

H_2O to the Ni^{3+} site in $\text{Ni}^{3+}-\text{O}$ species, thus promoting the chem-oxidation of HMF kinetically. Therefore, the as-fabricated $\text{V}_{\text{Mo}}\text{-NiO}_x\text{H}_y$ catalyst exhibits superior electrocatalytic activity on HMF and other substrates (alcohol and furfural) than pristine NiO_xH_y and delivers high HMF conversion efficiency with a FDCA yield and FE over 90% for at least 3 cycles. Our proposed strategy lays the foundation for future developments in high-performance electrocatalysts by providing valuable guidelines for the incorporation of cationic defects to enhance the pre-oxidation process and generate active sites.

CRediT authorship contribution statement

Zhao Lin: Visualization, Software. **Zhang Yagang:** Writing – review & editing, Writing – original draft, Validation, Supervision, Resources, Project administration, Funding acquisition, Formal analysis, Conceptualization. **Ma Xianhui:** Data curation. **Liu Yanxia:** Writing – review & editing. **Jiang Xiaoli:** Writing – original draft, Validation, Investigation, Formal analysis, Data curation, Conceptualization. **Zhang Qiang:** Writing – review & editing, Supervision, Formal analysis. **Li Bo-Quan:** Writing – review & editing, Validation, Formal analysis.

Declaration of Competing Interest

The authors declare that they have no known competing financial interests or personal relationships that could have appeared to influence the work reported in this paper. All authors state that there's no financial/personal interest or belief that could affect their objectivity.

Data Availability

Data will be made available on request.

Acknowledgments

This work was financially supported by Key Research and Development Projects of Sichuan Province (2023YFG0222), “Tianfu Emei” Science and Technology Innovation Leader Program in Sichuan Province (2021), University of Electronic Science and Technology of China Talent Start-up Funds (A1098, 5310, 2360, 1208), National Natural Science Foundation of China (21464015, 21472235).

Appendix A. Supporting information

Supplementary data associated with this article can be found in the online version at [doi:10.1016/j.apcatb.2024.123785](https://doi.org/10.1016/j.apcatb.2024.123785).

References

- W. Li, Z. Chen, X. Jiang, J. Jiang, Y. Zhang, Recent advances in the design of single-atom electrocatalysts by defect engineering, *Front. Chem.* 10 (2022) 1011597, <https://doi.org/10.3389/fchem.2022.1011597>.
- C.-X. Zhao, J.-N. Liu, J. Wang, D. Ren, J. Yu, X. Chen, B.-Q. Li, Q. Zhang, A $\Delta E = 0.63$ V bifunctional oxygen electrocatalyst enables high-rate and long-cycling zinc–air batteries, *Adv. Mater.* 33 (2021) 2008606, <https://doi.org/10.1002/adma.202008606>.
- W. Li, D. Wang, T. Liu, L. Tao, Y. Zhang, Y.-C. Huang, S. Du, C.-L. Dong, Z. Kong, Y.-f. Li, S. Lu, S. Wang, Doping-modulated strain enhancing the phosphate tolerance on PtFe alloys for high-temperature proton exchange membrane fuel cells, *Adv. Funct. Mater.* 32 (2022) 2109244, <https://doi.org/10.1002/adfm.202109244>.
- B.-Q. Li, S.-Y. Zhang, C. Tang, X. Cui, Q. Zhang, Anionic regulated NiFe (Oxy) sulfide electrocatalysts for water oxidation, *Small* 13 (2017) 1700610, <https://doi.org/10.1002/smll.201700610>.
- W. Li, L. Zhao, X. Jiang, Z. Chen, Y. Zhang, S. Wang, Confinement engineering of electrocatalyst surfaces and interfaces, *Adv. Funct. Mater.* 32 (2022) 2207727, <https://doi.org/10.1002/adfm.202207727>.
- X. Jiang, X. Yue, Y. Li, X. Wei, Q. Zheng, F. Xie, D. Lin, G. Qu, Anion-cation-dual doped tremella-like nickel phosphides for electrocatalytic water oxidation, *Chem. Eng. J.* 426 (2021) 130718, <https://doi.org/10.1016/j.cej.2021.130718>.
- C.-X. Zhao, B.-Q. Li, M. Zhao, J.-N. Liu, L.-D. Zhao, X. Chen, Q. Zhang, Precise anionic regulation of NiFe hydroxysulfide assisted by electrochemical reactions for efficient electrocatalysis, *Energy Environ. Sci.* 13 (2020) 1711–1716, <https://doi.org/10.1039/C9EE03573G>.
- Y.N. Palai, A. Shrotri, A. Fukuoka, Selective oxidation of furfural to succinic acid over Lewis acidic Sn-beta, *ACS Catal.* 12 (2022) 3534–3542, <https://doi.org/10.1021/acscatal.1c05348>.
- X. Liu, B. Li, G. Han, X. Liu, Z. Cao, D.-e Jiang, Y. Sun, Electrocatalytic synthesis of heterocycles from biomass-derived furfuryl alcohols, *Nat. Commun.* 12 (2021) 1868, <https://doi.org/10.1038/s41467-021-22157-5>.
- P. Zhou, X. Lv, S. Tao, J. Wu, H. Wang, X. Wei, T. Wang, B. Zhou, Y. Lu, T. Frauenheim, X. Fu, S. Wang, Y. Zou, Heterogeneous-interface-enhanced adsorption of organic and hydroxyl for biomass electrooxidation, *Adv. Mater.* 34 (2022) 2204089, <https://doi.org/10.1002/adma.202204089>.
- Y. Zhang, B. Zhou, Z. Wei, W. Zhou, D. Wang, J. Tian, T. Wang, S. Zhao, J. Liu, L. Tao, S. Wang, Coupling glucose-assisted Cu(I)/Cu(II) redox with electrochemical hydrogen production, *Adv. Mater.* 33 (2021) 2104791, <https://doi.org/10.1002/adma.202104791>.
- G. Yang, Y. Jiao, H. Yan, Y. Xie, A. Wu, X. Dong, D. Guo, C. Tian, H. Fu, Interfacial engineering of $\text{MoO}_2\text{-FeP}$ heterojunction for highly efficient hydrogen evolution coupled with biomass electrooxidation, *Adv. Mater.* 32 (2020) 2000455, <https://doi.org/10.1002/adma.202000455>.
- Y. Lu, C.-L. Dong, Y.-C. Huang, Y. Zou, S. Liu, Y. Liu, Y. Li, N. He, J. Shi, S. Wang, Identifying the Geometric Site Dependence of Spinel Oxides for the Electrooxidation of 5-Hydroxymethylfurfural, *Angew. Chem. Int. Ed.* 59 (2020) 19215–19221, <https://doi.org/10.1002/anie.202007767>.
- C. Xu, E. Paone, D. Rodríguez-Padrón, R. Luque, F. Mauriello, Recent catalytic routes for the preparation and the upgrading of biomass derived furfural and 5-hydroxymethylfurfural, *Chem. Soc. Rev.* 49 (2020) 4273–4306, <https://doi.org/10.1039/D0CS00041H>.
- M. Guo, X. Lu, J. Xiong, R. Zhang, X. Li, Y. Qiao, N. Ji, Z. Yu, Alloy-driven efficient electrocatalytic oxidation of biomass-derived 5-hydroxymethylfurfural towards 2,5-furandicarboxylic acid: a review, *ChemSusChem* 15 (2022) e202201074, <https://doi.org/10.1002/cssc.202201074>.
- J.N. Hausmann, R. Beltrán-Suito, S. Mebs, V. Hlukhyy, T.F. Fässler, H. Dau, M. Driess, P.W. Menezes, Evolving highly active oxidic iron(III) phase from corrosion of intermetallic iron silicide to master efficient electrocatalytic water oxidation and selective oxygenation of 5-hydroxymethylfurfural, *Green Chem.* 33 (2021) 2008823, <https://doi.org/10.1002/adma.202008823>.
- X.-J. Bai, W.-X. He, X.-Y. Lu, Y. Fu, W. Qi, Electrochemical oxidation of 5-hydroxymethylfurfural on ternary metal-organic framework nanoarrays: enhancement from electronic structure modulation, *J. Mater. Chem. A* 9 (2021) 14270–14275, <https://doi.org/10.1039/DITA02464G>.
- F. Li, Y. Li, K.S. Novoselov, F. Liang, J. Meng, S.-H. Ho, T. Zhao, H. Zhou, A. Ahmad, Y. Zhu, L. Hu, D. Ji, L. Jia, R. Liu, S. Ramakrishna, X. Zhang, Bioresource upgrade for sustainable energy, environment, and biomedicine, *Nano-Micro Lett.* 15 (2023) 35, <https://doi.org/10.1007/s40820-022-00993-4>.
- Y. Lu, T. Liu, C.-L. Dong, C. Yang, L. Zhou, Y.-C. Huang, Y. Li, B. Zhou, Y. Zou, S. Wang, Tailoring competitive adsorption sites by oxygen-vacancy on cobalt oxides to enhance the electrooxidation of biomass, *Adv. Mater.* 34 (2022) 2107185, <https://doi.org/10.1002/adma.202107185>.
- G. Kresse, J. Hafner, Ab initio molecular dynamics for open-shell transition metals, *Phys. Rev. B* 48 (1993) 13115–13118, <https://doi.org/10.1103/PhysRevB.48.13115>.
- G. Kresse, J. Furthmüller, Efficient iterative schemes for ab initio total-energy calculations using a plane-wave basis set, *Phys. Rev. B* 54 (1996) 11169–11186, <https://doi.org/10.1103/PhysRevB.54.11169>.
- P.E. Blöchl, Projector augmented-wave method, *Phys. Rev. B* 50 (1994) 17953–17979, <https://doi.org/10.1103/PhysRevB.50.17953>.
- G. Kresse, D. Joubert, From ultrasoft pseudopotentials to the projector augmented-wave method, *Phys. Rev. B* 59 (1999) 1758–1775, <https://doi.org/10.1103/PhysRevB.59.1758>.
- P. Hohenberg, W. Kohn, Inhomogeneous electron gas, *Phys. Rev.* 136 (1964) B864–B871, <https://doi.org/10.1103/PhysRev.136.B864>.
- W. Kohn, L.J. Sham, Self-consistent equations including exchange and correlation effects, *Phys. Rev.* 140 (1965) A1133–A1138, <https://doi.org/10.1103/PhysRev.140.A1133>.
- J. VandeVondele, M. Krack, F. Mohamed, M. Parrinello, T. Chassaing, J. Hutter, Quickstep: fast and accurate density functional calculations using a mixed Gaussian and plane waves approach, *Comput. Phys. Commun.* 167 (2005) 103–128, <https://doi.org/10.1016/j.cpc.2004.12.014>.
- S. Goedecker, M. Teter, J. Hutter, Separable dual-space gaussian pseudopotentials, *Phys. Rev. B* 54 (1996) 1703–1710, <https://doi.org/10.1103/PhysRevB.54.1703>.
- C. Hartwigsen, S. Goedecker, J. Hutter, Relativistic separable dual-space gaussian pseudopotentials from H to Rn, *Phys. Rev. B* 58 (1998) 3641–3662, <https://doi.org/10.1103/PhysRevB.58.3641>.
- M. Krack, M. Parrinello, All-electron ab-initio molecular dynamics, *Phys. Chem. Chem. Phys.* 2 (2000) 2105–2121, <https://doi.org/10.1039/b001167n>.
- J. VandeVondele, J. Hutter, Gaussian basis sets for accurate calculations on molecular systems in gas and condensed phases, *J. Chem. Phys.* 127 (2007) 114105, <https://doi.org/10.1063/1.2770708>.
- J.P. Perdew, K. Burke, M. Ernzerhof, Generalized gradient approximation made simple, *Phys. Rev. Lett.* 77 (1996) 3865.
- S. Grimme, J. Antony, S. Ehrlich, H. Krieg, A consistent and accurate ab initio parametrization of density functional dispersion correction (DFT-D) for the 94 elements H–Pu, *J. Chem. Phys.* 132 (2010) 154104, <https://doi.org/10.1063/1.3382344>.

[33] J. Lv, L. Wang, R. Li, K. Zhang, D. Zhao, Y. Li, X. Li, X. Huang, G. Wang, Constructing a hetero-interface composed of oxygen vacancy-enriched Co_3O_4 and crystalline-amorphous NiFe-LDH for oxygen evolution reaction, *ACS Catal.* 11 (2021) 14338–14351, <https://doi.org/10.1021/acsata.1c03960>.

[34] G. Qian, J. Chen, T. Yu, J. Liu, L. Luo, S. Yin, Three-phase heterojunction NiMo-based nano-needle for water splitting at industrial alkaline condition, *Nano-Micro Lett.* 14 (2021) 20, <https://doi.org/10.1007/s40820-021-00744-x>.

[35] B. Cui, M. Zhang, Y. Zhao, S. Hu, Heterogenization of few-layer MoS_2 with highly crystalline 3D Ni_3S_2 nanoframes effectively synergizes the electrocatalytic hydrogen generation in alkaline medium, *Mater. Today Energy* 13 (2019) 85–92, <https://doi.org/10.1016/j.mtener.2019.05.001>.

[36] J. Staszak-Jirkovský, Christos D. Malliakas, Pietro P. Lopes, N. Danilovic, Subrahmanyam S. Kota, K.-C. Chang, B. Genorio, D. Strmcnik, Vojislav R. Stamenkovic, M.G. Kanatzidis, N.M. Markovic, Design of active and stable Co–Mo–S_x chalcogels as pH-universal catalysts for the hydrogen evolution reaction, *Nat. Mater.* 15 (2016) 197–203, <https://doi.org/10.1038/nmat4481>.

[37] X. Wang, J. Wang, X. Sun, S. Wei, L. Cui, W. Yang, J. Liu, Hierarchical coral-like NiMoS nanohybrids as highly efficient bifunctional electrocatalysts for overall urea electrolysis, *Nano Res* 11 (2018) 988–996, <https://doi.org/10.1007/s12274-017-1711-3>.

[38] W. Wang, L. Yang, F. Qu, Z. Liu, G. Du, A.M. Asiri, Y. Yao, L. Chen, X. Sun, A self-supported NiMoS₄ nanoarray as an efficient 3D cathode for the alkaline hydrogen evolution reaction, *J. Mater. Chem. A* 5 (2017) 16585–16589, <https://doi.org/10.1039/C7TA05521H>.

[39] H. Yang, L. Gong, H. Wang, C. Dong, J. Wang, K. Qi, H. Liu, X. Guo, B.Y. Xia, Preparation of nickel-iron hydroxides by microorganism corrosion for efficient oxygen evolution, *Nat. Commun.* 11 (2020) 5075, <https://doi.org/10.1038/s41467-020-18891-x>.

[40] C.-X. Zhao, J.-N. Liu, C. Wang, J. Wang, L. Song, B.-Q. Li, Q. Zhang, An anionic regulation mechanism for the structural reconstruction of sulfide electrocatalysts under oxygen evolution conditions, *Energy Environ. Sci.* 15 (2022) 3257–3264, <https://doi.org/10.1039/D2EE01036D>.

[41] H. Zhong, Q. Zhang, J. Yu, X. Zhang, C. Wu, Y. Ma, H. An, H. Wang, J. Zhang, X. Wang, J. Xue, Fundamental understanding of structural reconstruction behaviors in oxygen evolution reaction electrocatalysts, *Adv. Energy Mater.* 13 (2023) 2301391, <https://doi.org/10.1002/aenm.202301391>.

[42] X. Liu, J. Meng, J. Zhu, M. Huang, B. Wen, R. Guo, L. Mai, Comprehensive understandings into complete reconstruction of precatalysts: synthesis, applications, and characterizations, *Adv. Mater.* 33 (2021) 2007344, <https://doi.org/10.1002/adma.202007344>.

[43] C. Guo, Y. Shi, S. Lu, Y. Yu, B. Zhang, Amorphous nanomaterials in electrocatalytic water splitting, *Chin. J. Catal.* 42 (2021) 1287–1296, [https://doi.org/10.1016/S1872-2067\(20\)63740-8](https://doi.org/10.1016/S1872-2067(20)63740-8).

[44] F. Gunkel, D.V. Christensen, Y.Z. Chen, N. Pryds, Oxygen vacancies: the (in)visible friend of oxide electronics, *Appl. Phys. Lett.* 116 (2020) 120505, <https://doi.org/10.1063/1.5143309>.

[45] P. Wang, Y. Luo, G. Zhang, Z. Chen, H. Ranganathan, S. Sun, Z. Shi, Interface engineering of $\text{Ni}_3\text{S}_2@\text{MnO}_x\text{H}_y$ nanorods to efficiently enhance overall-water-splitting activity and stability, *Nano-Micro Lett.* 14 (2022) 120, <https://doi.org/10.1007/s40820-022-00860-2>.

[46] E. Fabbri, M. Nachtegaal, T. Binninger, X. Cheng, B.-J. Kim, J. Durst, F. Bozza, T. Graule, R. Schäublin, L. Wiles, M. Pertoso, N. Danilovic, K.E. Ayers, T. J. Schmidt, Dynamic surface self-reconstruction is the key of highly active perovskite nano-electrocatalysts for water splitting, *Nat. Mater.* 16 (2017) 925–931, <https://doi.org/10.1038/nmat4938>.

[47] J. Li, J. Li, J. Ren, H. Hong, D. Liu, L. Liu, D. Wang, Electric-field-treated Ni/Co₃O₄ film as high-performance bifunctional electrocatalysts for efficient overall water splitting, *Nano-Micro Lett.* 14 (2022) 148, <https://doi.org/10.1007/s40820-022-00889-3>.

[48] J. Ge, Y. Chen, Y. Zhao, Y. Wang, F. Zhang, X. Lei, Activated MoS₂ by constructing single atomic cation vacancies for accelerated hydrogen evolution reaction, *ACS Appl. Mater. Interfaces* 14 (2022) 26846–26857, <https://doi.org/10.1021/acsami.2c06708>.

[49] R. Zhou, S. Yang, T. E. L. Liu, J. Qian, The defect is perfect: MoS₂/TiO₂ modified with unsaturated Mo vacancies to construct Z-scheme heterojunction & improve mobility of e⁻, *J. Clean. Prod.* 337 (2022) 130511, <https://doi.org/10.1016/j.jclepro.2022.130511>.

[50] P. Gu, L. Bai, L. Gao, R. Brousseau, B.E. Conway, Problems in the determination of adsorption behaviour of intermediates in faradaic reactions: Distinction between double layer and adsorption capacitance of electrocatalysts determined from fast potential relaxation transients, *Electrochim. Acta* 37 (1992) 2145–2154, [https://doi.org/10.1016/0013-4686\(92\)85105-T](https://doi.org/10.1016/0013-4686(92)85105-T).

[51] C. Huang, Y. Huang, C. Liu, Y. Yu, B.J.A.C. Zhang, Integrating hydrogen production with aqueous selective semi-dehydrogenation of tetrahydroisoquinolines over a Ni₂P bifunctional electrode, *Angew. Chem. Int. Ed.* 131 (2019) 12142–12145.

[52] J. Huang, Y. Li, Y. Zhang, G. Rao, C. Wu, Y. Hu, X. Wang, R. Lu, Y. Li, J.J.A. C. Xiong, Identification of key reversible intermediates in self-reconstructed nickel-based hybrid electrocatalysts for oxygen evolution, *Angew. Chem. Int. Ed.* 131 (2019) 17619–17625.

[53] B. Zhou, C.-L. Dong, Y.-C. Huang, N. Zhang, Y. Wu, Y. Lu, X. Yue, Z. Xiao, Y. Zou, S. Wang, Activity origin and alkalinity effect of electrocatalytic biomass oxidation on nickel nitride, *J. Energy Chem.* 61 (2021) 179–185, <https://doi.org/10.1016/j.jechem.2021.02.026>.

[54] W. Chen, C. Xie, Y. Wang, Y. Zou, C.-L. Dong, Y.-C. Huang, Z. Xiao, Z. Wei, S. Du, C. Chen, B. Zhou, J. Ma, S. Wang, Activity origins and design principles of nickel-based catalysts for nucleophilic electroxidation, *Chem* 6 (2020) 2974–2993, <https://doi.org/10.1016/j.chempr.2020.07.022>.

[55] R. Subbaraman, D. Tripkovic, K.-C. Chang, D. Strmcnik, A.P. Paulikas, P. Hirunsit, M. Chan, J. Greeley, V. Stamenkovic, N.M. Markovic, Trends in activity for the water electrolysis reactions on 3d M(Ni,Co,Fe,Mn) hydr(oxy)oxide catalysts, *Nat. Mater.* 11 (2012) 550–557, <https://doi.org/10.1038/nmat3313>.

[56] Y. Shao, X. Xiao, Y.-P. Zhu, T.-Y. Ma, Single-crystal cobalt phosphate nanosheets for biomimetic oxygen evolution in neutral electrolytes, *Angew. Chem. Int. Ed.* 58 (2019) 14599–14604, <https://doi.org/10.1002/anie.201909326>.

[57] R. Ge, Y. Wang, Z. Li, M. Xu, S.-M. Xu, H. Zhou, K. Ji, F. Chen, J. Zhou, H. Duan, Selective electroxidation of biomass-derived alcohols to aldehydes in a neutral medium: promoted water dissociation over a nickel-oxide-supported ruthenium single-atom catalyst, *Angew. Chem. Int. Ed.* 61 (2022) e202200211, <https://doi.org/10.1002/anie.202200211>.

[58] D.R. Pradhan, S. Pattaik, J. Kishore, C. Gunanathan, Cobalt-catalyzed acceptorless dehydrogenation of alcohols to carboxylate salts and hydrogen, *Org. Lett.* 22 (2020) 1852–1857, <https://doi.org/10.1021/acs.orglett.0c00193>.

[59] X. Wu, N. Luo, S. Xie, H. Zhang, Q. Zhang, F. Wang, Y. Wang, Photocatalytic transformations of lignocellulosic biomass into chemicals, *Chem. Soc. Rev.* 49 (2020) 6198–6223, <https://doi.org/10.1039/DOCS00314J>.

[60] H.-Y. Wang, S.-F. Hung, H.-Y. Chen, T.-S. Chan, H.M. Chen, B. Liu, In operando identification of geometrical-site-dependent water oxidation activity of spinel Co_3O_4 , *J. Am. Chem. Soc.* 138 (2016) 36–39, <https://doi.org/10.1021/jacs.5b10525>.

[61] W. Chen, Y. Wang, B. Wu, J. Shi, Y. Li, L. Xu, C. Xie, W. Zhou, Y.-C. Huang, T. Wang, S. Du, M. Song, D. Wang, C. Chen, J. Zheng, J. Liu, C.-L. Dong, Y. Zou, J. Chen, S. Wang, Activated Ni–OH Bonds in a Catalyst Facilitates the Nucleophilic Oxidation Reaction, *Adv. Mater.* 34 (2022) 2105320, <https://doi.org/10.1002/adma.202105320>.

[62] J. Wu, Z. Kong, Y. Li, Y. Lu, P. Zhou, H. Wang, L. Xu, S. Wang, Y. Zou, Unveiling the adsorption behavior and redox properties of PtNi nanowire for biomass-derived molecules electroxidation, *ACS Nano* 16 (2022) 21518–21526, <https://doi.org/10.1021/acsnano.2c10327>.

[63] Y. Lu, C.-L. Dong, Y.-C. Huang, Y. Zou, Y. Liu, Y. Li, N. Zhang, W. Chen, L. Zhou, H. Lin, S. Wang, Hierarchically nanostructured $\text{NiO}-\text{Co}_3\text{O}_4$ with rich interface defects for the electro-oxidation of 5-hydroxymethylfurfural, *Sci. China Chem.* 63 (2020) 980–986, <https://doi.org/10.1007/s11426-020-9749-8>.

[64] M. Fleischmann, K. Korinek, D. Pletcher, The oxidation of organic compounds at a nickel anode in alkaline solution, *J. Electroanal. Chem. Interfacial Electrochem.* 31 (1971) 39–49, [https://doi.org/10.1016/S0022-0728\(71\)80040-2](https://doi.org/10.1016/S0022-0728(71)80040-2).

[65] M.T. Bender, K.-S. Choi, Electrochemical oxidation of HMF via hydrogen atom transfer and hydride transfer on NiOOH and the impact of NiOOH composition, *ChemSusChem* 15 (2022) e202200675, <https://doi.org/10.1002/cssc.202200675>.

[66] N. Zhang, Y. Zou, L. Tao, W. Chen, L. Zhou, Z. Liu, B. Zhou, G. Huang, H. Lin, S. Wang, Electrochemical oxidation of 5-hydroxymethylfurfural on nickel nitride/carbon nanosheets: reaction pathway determined by in situ sum frequency generation vibrational spectroscopy, *Angew. Chem. Int. Ed.* 58 (2019) 15895–15903, <https://doi.org/10.1002/anie.201908722>.